Research Article | Vol. 25, No. 16 | 7 Aug 2017 | OPTICS EXPRESS 18842
Optics EXPRESS

Experimental measurement of supercontinuum coherence in highly nonlinear soft-glass photonic crystal fibers

YUJI ZHANG,[1] JANA KAINERSTORFER,[2] JONATHAN C. KNIGHT,[3] AND FIORENZO G. OMENETTO[1,2,*]

[1]*Tufts University, Department of Physics and Astronomy, 4 Colby St, Medford, MA 02155, USA*
[2]*Tufts University, Department of Biomedical Engineering, 4 Colby St, Medford, MA 02155, USA*
[3]*Centre for Photonics and Photonic Materials, Department of Physics, University of Bath, UK*
[*]*fiorenzo.omenetto@tufts.edu*

Abstract: We present experimental measurements illustrating the power-dependent coherence evolution for supercontinuum generated in highly nonlinear SF6 photonic crystal fibers. The measurements were performed for fiber lengths close to and much longer than the soliton fission length. Simulations of the spectral evolution were also carried out to accompany the experimental observation. Many parameters were estimated by matching the simulated and the measured evolution. Both the measured and the simulated coherence evolution confirm the association between coherence degradation and soliton fission.

OCIS codes: (190.3270) Kerr effect; (190.5650) Raman effect; (060.4370) Nonlinear optics, fibers; (060.5295) Photonic crystal fibers; (320.6629) Supercontinuum generation; (030.1640) Coherence.

References and links

1. J. M. Dudley, G. Genty, and S. Coen, "Supercontinuum generation in photonic crystal fiber," Rev. Mod. Phys. **78**(4), 1135–1184 (2006).
2. W. H. Reeves, D. V. Skryabin, F. Biancalana, J. C. Knight, P. St. J. Russell, F. G. Omenetto, A. Efimov, and A. J. Taylor, "Transformation and control of ultra-short pulses in dispersion-engineered photonic crystal fibres," Nature **424**(6948), 511–515 (2003).
3. G. Tao, A. M. Stolyarov, and A. F. Abouraddy, "Multimaterial Fibers," Int. J. Appl. Glass Sci. **3**(4), 349–368 (2012).
4. V. V. Kumar, A. George, W. Reeves, J. Knight, P. Russell, F. Omenetto, and A. Taylor, "Extruded soft glass photonic crystal fiber for ultrabroad supercontinuum generation," Opt. Express **10**(25), 1520–1525 (2002).
5. F. G. Omenetto, N. A. Wolchover, M. R. Wehner, M. Ross, A. Efimov, A. J. Taylor, V. V. R. K. Kumar, A. K. George, J. C. Knight, N. Y. Joly, and P. St. J. Russell, "Spectrally smooth supercontinuum from 350 nm to 3 mum in sub-centimeter lengths of soft-glass photonic crystal fibers," Opt. Express **14**(11), 4928–4934 (2006).
6. J. T. Moeser, N. A. Wolchover, J. C. Knight, and F. G. Omenetto, "Initial dynamics of supercontinuum generation in highly nonlinear photonic crystal fiber," Opt. Lett. **32**(8), 952–954 (2007).
7. K. L. Corwin, N. R. Newbury, J. M. Dudley, S. Coen, S. A. Diddams, K. Weber, and R. S. Windeler, "Fundamental Noise Limitations to Supercontinuum Generation in Microstructure Fiber," Phys. Rev. Lett. **90**(11), 113904 (2003).
8. J. M. Dudley and S. Coen, "Coherence properties of supercontinuum spectra generated in photonic crystal and tapered optical fibers," Opt. Lett. **27**(13), 1180–1182 (2002).
9. X. Gu, M. Kimmel, A. Shreenath, R. Trebino, J. Dudley, S. Coen, and R. Windeler, "Experimental studies of the coherence of microstructure-fiber supercontinuum," Opt. Express **11**(21), 2697–2703 (2003).
10. F. Lu and W. Knox, "Generation of a broadband continuum with high spectral coherence in tapered single-mode optical fibers," Opt. Express **12**(2), 347–353 (2004).
11. J. Nicholson and M. Yan, "Cross-coherence measurements of supercontinua generated in highly-nonlinear, dispersion shifted fiber at 1550 nm," Opt. Express **12**(4), 679–688 (2004).
12. S. M. Kobtsev, S. V. Kukarin, N. V. Fateev, and S. V. Smirnov, "Coherent, polarization and temporal properties of self-frequency shifted solitons generated in polarization-maintaining microstructured fibre," Appl. Phys. B **81**(2), 265–269 (2005).
13. I. Zeylikovich, V. Kartazaev, and R. R. Alfano, "Spectral, temporal, and coherence properties of supercontinuum generation in microstructure fiber," J. Opt. Soc. Am. B **22**(7), 1453–1460 (2005).
14. D. Türke, S. Pricking, A. Husakou, J. Teipel, J. Herrmann, and H. Giessen, "Coherence of subsequent supercontinuum pulses generated in tapered fibers in the femtosecond regime," Opt. Express **15**(5), 2732–2741 (2007).

#290954 https://doi.org/10.1364/OE.25.018842
Journal © 2017 Received 19 May 2017; revised 20 Jul 2017; accepted 24 Jul 2017; published 26 Jul 2017

Optics EXPRESS

15. A. M. Heidt, A. Hartung, G. W. Bosman, P. Krok, E. G. Rohwer, H. Schwoerer, and H. Bartelt, "Coherent octave spanning near-infrared and visible supercontinuum generation in all-normal dispersion photonic crystal fibers," Opt. Express **19**(4), 3775–3787 (2011).
16. S. T. Sørensen, O. Bang, B. Wetzel, and J. M. Dudley, "Describing supercontinuum noise and rogue wave statistics using higher-order moments," Opt. Commun. **285**(9), 2451–2455 (2012).
17. B. Wetzel, A. Stefani, L. Larger, P. A. Lacourt, J. M. Merolla, T. Sylvestre, A. Kudlinski, A. Mussot, G. Genty, F. Dias, and J. M. Dudley, "Real-time full bandwidth measurement of spectral noise in supercontinuum generation," Sci. Rep. **2**, 882 (2012).
18. M. Närhi, J. Turunen, A. T. Friberg, and G. Genty, "Experimental Measurement of the Second-Order Coherence of Supercontinuum," Phys. Rev. Lett. **116**(24), 243901 (2016).
19. D. R. Solli, C. Ropers, P. Koonath, and B. Jalali, "Optical rogue waves," Nature **450**(7172), 1054–1057 (2007).
20. J. M. Dudley and J. R. Taylor, *Supercontinuum Generation in Optical Fibers*, 1st ed. (Cambridge University, 2010).
21. M. H. Frosz, "Validation of input-noise model for simulations of supercontinuum generation and rogue waves," Opt. Express **18**(14), 14778–14787 (2010).

1. Introduction

Supercontinuum (SC) generation in photonic crystal fibers (PCF) has been a widely studied field of great interest and wide applications [1]. The microstructures present in the PCF enhance nonlinearity and allow for engineering the dispersion properties [2]. The fiber material [3] and the fiber length are also important factors. For example, Schott SF6 glass has a nonlinear refractive index (n_2) almost 10 times higher than that of fused silica, and is useful for ultrabroad SC generation [4]. When the fiber length is shorter than the soliton fission length (L_{fiss}), SC is based nearly purely on self phase modulation (SPM), and soliton fission is avoided. This approach was previously used in SF6 to generate broad (350–3000 nm) spectrally smooth SC [5]. The spectral smoothness in this case was attributed to the stability of this SPM-dominated SC, not due to averaging in the measurement [6].

The stability of SC has been studied quite extensively. Previous results have characterized it in terms of the radio-frequency noise [7], in terms of the pulse-to-pulse coherence $|g_{12}^{(1)}|$ [8–15], in terms of the pulse-to-pulse fluctuation of spectral intensity [16, 17], and in terms of second order coherence [18]. The connection between the noise properties of SC and the formation of rogue waves has also been studied [19].

Coherence evolution has been previously used to visualize SC coherence dynamics [1]. However, most previous experimental research measured coherence under only a limited collection of conditions, e.g., a few levels of SC power.

In this paper, we present the results obtained from experimentally measured spectral evolution $I(\lambda,P)$ and coherence evolution $|g_{12}^{(1)}(\lambda,P)|$ (where λ is the wavelength and P is the average power of SC). PCFs of lengths much longer ($L_{fiber} >> L_{fiss}$) and comparable to ($L_{fiber} \sim L_{fiss}$) the soliton fission length were used to investigate the dependence of coherence on the fiber length. Numerical simulations were also performed to correlate with the experimental results. The stability of spectral intensity is compared to the coherence in simulations.

2. Experiment

The SF6 PCF used in the experiment is shown in the inset of Fig. 1. The core diameter is 3.6 μm. Assuming the effective mode area A_{eff} = core area = 10.18 μm^2, the nonlinear coefficient of the fiber is calculated to be $\gamma = 2\pi n_2 / \lambda_0 A_{eff}$ = 87.6/km·W, where $n_2 = 2.2 \times 10^{-19}$ m^2/W is the nonlinear refractive index of SF6 glass, and λ_0 = 1550 nm is the pump wavelength. Three fiber lengths were used for the experiments: 10.5 cm, 4.7 mm, and 3.9 mm.

Figure 1 shows the experimental setup. An optical parametric oscillator (OPO, Spectra-Physics Opal) is pumped by a mode-locked Ti:sapphire laser. The OPO generates pulses at λ_0 = 1550 nm, of duration $T_{FWHM} \sim$ 105 fs, at a repetition rate f_{rep} = 80 MHz, and with an average power P = 250 mW.

Optics EXPRESS

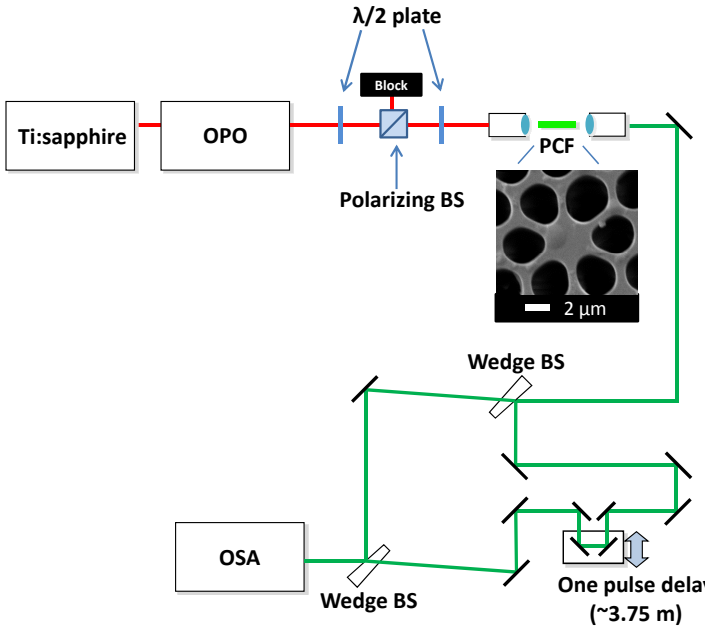

Fig. 1. Experimental setup for the measurement of the coherence between successive SC pulses. A "long-arm" interferometer generating a one pulse delay allows successive SC pulses to overlap temporally. The inset is the scanning electron microscopy (SEM) image of the facet of the SF6 PCF used in the experiment. The core diameter is 3.6 μm. BS = beam splitter; OPO = optical parametric oscillator; and OSA = optical spectrum analyzer.

A combination of a half wave plate and a polarizing beam splitter was used to tune the laser power sent into the PCF. Another half wave plate was used to tune the polarization of the laser. A 60X aspherical lens was used to couple the laser into the PCF, and another was used for collimation. At the maximum pump power (~250 mW), the average power of SC was measured to be 80 mW, corresponding to a coupling efficiency approaching 30%.

A Mach-Zehnder (MZ) interferometer with a long delay arm was built to allow to interfere successive SC pulses (Fig. 1). By using wedge beam splitters, instead of plate/cube/pellicle beam splitters, ghosting was mitigated. The interference signal was measured by an optical spectrum analyzer (OSA, Yokogawa AQ6370B) with a wavelength range of 600–1700 nm.

The detected signal $I_{12}(\lambda)$ shows interference fringes with a visibility (or contrast) described by

$$V(\lambda)=\frac{2\left[I_1(\lambda)I_2(\lambda)\right]^{1/2}}{I_1(\lambda)+I_2(\lambda)}\left|g_{12}^{(1)}(\lambda)\right| \qquad (1)$$

in which $I_1(\lambda)$ and $I_2(\lambda)$ are the SC spectra of the short- and the long-arm beam, respectively. The fringe visibility $V(\lambda)$ was extracted from $I_{12}(\lambda)$, and then the coherence $|g_{12}^{(1)}(\lambda)|$ was calculated using Eq. (1). By tuning the power coupled into the fiber, the power-dependent coherence evolution $|g_{12}^{(1)}(\lambda,P)|$ was obtained, where P is the average power of SC obtained by measuring the collimated output from the fiber. The spectral evolution of SC is just $I_1(\lambda,P)$ or $I_2(\lambda,P)$, measured by blocking one of the arms in the interferometer. Here the short-arm signal $I_1(\lambda,P)$ is used, because it has less divergence and higher intensity. Spectrally averaged coherence

Optics EXPRESS

$$\left\langle \left| g_{12}^{(1)}(P) \right| \right\rangle = \frac{\sum_{\lambda} \left| g_{12}^{(1)}(\lambda, P) \right| \cdot I_1(\lambda, P)}{\sum_{\lambda} I_1(\lambda)} \tag{2}$$

was calculated to represent the overall coherence [1].

3. Results

The experimental results are shown in Fig. 2. The data is obtained using three different lengths of SF6 PCFs: Fig. 2(a)–2(c) represent the spectral evolution as a function of power, Fig. 2(d)–2(f) the corresponding coherence evolution, and Fig. 2(g)–2(i) are representative spectra taken at different powers for each case.

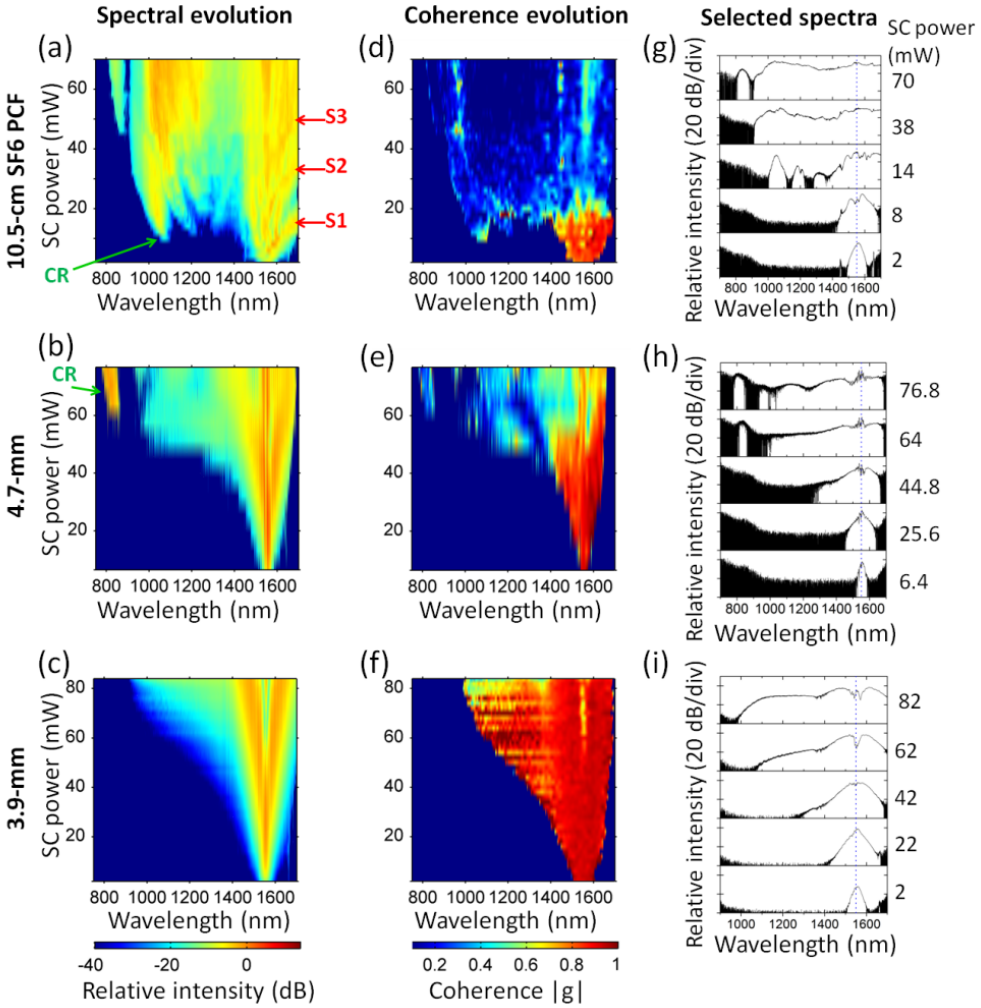

Fig. 2. Spectral evolution (a)–(c) and coherence evolution (d)–(f) of SC generated in three different lengths of SF6 PCFs (10.5-cm, 4.7-mm, and 3.9-mm). S1–S3 in (a) mark solitons. CR in (a) and (b) marks Cherenkov radiation. The spectral evolution is calibrated such that the maximum intensity is 0 dB. (g)–(i) are representative spectra.

In the case using the 10.5-cm SF6 PCF, the spectral evolution [Fig. 2(a)] shows a soliton-fission-dominated pattern. Ejection of the first soliton (indicated by S1 in the figure) occurs at

Optics EXPRESS

~10 mW, accompanied with the emergence of the Cherenkov peak at ~1070 nm (CR in the figure). Solitons (S1–S3 in the figure) show Raman-induced red shift. The coherence [Fig. 2(d)] is high for the initial broadening, and degrades quickly after soliton fission has occurred.

For the case of the 4.7-mm fiber [Fig. 2(b)] the SC presents two symmetric spectral lobes at both sides of the pump wavelength for power less than ~45 mW, indicative of a self-phase-modulation dominated regime. At ~45 mW, strong spectral broadening occurs, which is related to temporal compression and should precede soliton fission. Although no clear soliton trajectory was captured, the Cherenkov peak emerging at ~850 nm ~60 mW (CR in the figure) provides some evidence of the presence of a corresponding soliton. The coherence properties [Fig. 2(e)] follow this trend: high coherence (~0.9) was maintained for power less than ~45 mW (before soliton fission). For powers higher than ~45 mW (after soliton fission), coherence degradation occurs at most parts of the spectrum.

For the shortest (z = 3.9 mm) PCF case, the blue end of the spectrum approaches ~1000 nm at P ~75 mW [Fig. 2(c)], similar to the situation at P ~50 mW in the 4.7-mm case [Fig. 2(b)]. This is indicative of the temporal compression preceding soliton fission. At the same time, coherence degradation starts to occur at wavelengths far from the pump [at P ~75 mW in Fig. 2(f)]. It is expected that, for P > 84 mW, the dynamics should be similar to what happens at P > ~50 mW in the 4.7-mm case. Unfortunately, such dynamics were not measured, due to the limited power of the pump.

The above results visualize the correlation between coherence degradation and soliton fission. Using a fiber slightly shorter than the soliton fission length, SC of high coherence can be generated while maximizing bandwidth (i.e., the 3.9-mm fiber case).

We expect the spectral and coherence dynamics in the 3.9-mm case similar to those of the P < ~50 mW part in the 4.7-mm case. A discrepancy in the spectral extent of high coherence in the 4.7-mm fiber is observed, with the SC coherence not extending to ~1000 nm, as in the 3.9-mm case [Fig. 2(e) vs. 2(f)]. This is attributed to the fact that the 4.7-mm case was measured with lower sensitivity in the spectral detection apparatus, making the noise floor closer to the spectra [see Fig. 2(h), compared with 2(g) and 2(i)]. We do expect that higher sensitivity settings would eliminate these issues.

To compare experimental results to the theory, the SC generation was modeled with the frequency-domain generalized nonlinear Schrödinger equation (GNLSE) [1,20].

The GVD curve of the 3.6-μm-core PCF fiber used in the experiments (denoted $\beta_2(\omega)|_{3.6\text{-}\mu m}$) was estimated by linearly interpolating the measured GVDs of a 2.6-μm-core and a 4-μm-core SF6 PCF reported in [4], yielding $\beta_2(\omega_0)$ = –48.39 ps^2/km and $\beta_3(\omega_0)$ = 0.305 ps^3/km, where $\beta_2(\omega_0)$ and $\beta_2(\omega_0)$ are the Taylor expansion coefficients of the wave number $\beta_n(\omega_0) = \left(d^n\beta/d\omega^n\right)_{\omega_0}$. It is worth noting that the fibers of 2.6-μm core and 4-μm core diameters in [4] have a different microstructure than our fiber, inevitably leading to some uncertainty in the estimation.

The modeling yields calculated values of $\beta_2(\omega_0)$ = –96.78 ps^2/km, and a corresponding L_{fiss} = 5.4 mm at P = 77 mW. This value favorably compares with the experimental measurements where the soliton fission length is between 3.9 and 4.7 mm.

The soliton number was estimated to be N~6 at soliton fission. This value is relatively small compared to previous results [1], which may be due to uncertainties in the parameters estimation. The simulated spectral evolution is plotted in Fig. 3 and shows, as expected, good qualitative agreement with the measurement.

Optics EXPRESS

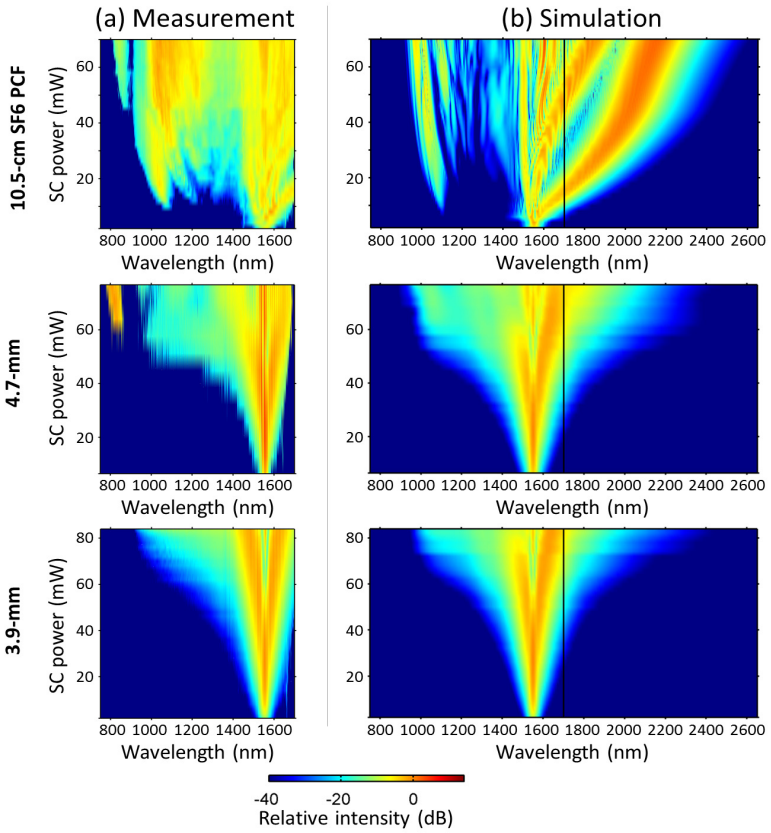

Fig. 3. (a) Measured and (b) simulated spectral evolution using three different lengths of SF6 PCFs. The simulation plots have black lines at 1700 nm to help visual comparison between experiment and simulation. Comparison between measurement and simulation shows agreement in the broadening trends, in the soliton fission powers, and in the emergence of Cherenkov radiation.

Some differences in the results are affected by the inability to assign the appropriate experimental values to the simulation. In the 10.5-cm case, for example, the experiments and the simulations show agreement in the trajectory of the first soliton, but some discrepancies in the second and the third ones. The soliton wavelength is determined by the Raman-induced frequency shift $\Omega \propto |\beta_2| z / T_0^4$, in which T_0 is the duration of the soliton. The mismatch can be explained by discrepancies in the soliton pulse width, especially considering the inverse quartic dependence. Consequently, given that the Cherenkov radiation is phase matched with solitons [1], possible inaccuracy in the soliton wavelengths and in the dispersion also affect the discrepancies between experimental and simulated results.

The nonlinear transformation that pulses are subject to during propagation through short PCFs makes them susceptible to small variations in the input pulse characteristics. It is worth noting that small fluctuations (such as amplitude noise) in the input pulses may contribute to confound the physics of this highly nonlinear transformation process. This remains a challenge to be addressed when attempting to control the spectral quality and stability of PCF-based SC sources.

The coherence was simulated by adding noise into the model. Previously used models have simulated a one-photon-per-mode shot noise [1], a phase-diffusion-based noise [21], or simulated pulse-to-pulse fluctuation of the pump power [1]. Here we applied a simple model

Optics EXPRESS

including the one-photon-per-mode noise and pulse power fluctuation. Specifically, the peak power of a pump pulse is $P_0 = \overline{P}_0 \cdot \Delta_P$, where $\overline{P}_0$ is the average peak power of the pump pulses, and Δ_P has a Gaussian distribution of a mean = 0 and a standard deviation of 5%.

Coherence is calculated from the simulated optical field $E(\lambda)$ using [1]

$$\left|g_{12}(\lambda)\right| = \frac{\left|\left\langle E_m^*(\lambda)E_n(\lambda)\right\rangle_{m\neq n}\right|}{\left[\left\langle\left|E_m(\lambda)\right|^2\right\rangle_m \left\langle\left|E_n(\lambda)\right|^2\right\rangle_n\right]^{1/2}} = \frac{\left|\sum_{m\neq n} E_m^*(\lambda)E_n(\lambda)\Big/\left[N(N-1)\right]\right|}{\sum_m \left|E_m(\lambda)\right|^2 \Big/ N} \tag{3}$$

in which m, n = 1, 2, …, N, ⟨ ⟩ denotes the ensemble average, and an ensemble of 20 pulses was used (N = 20).

The coherence can be determined by pulse-to-pulse phase correlation and pulse-to-pulse stability of spectral intensity. To isolate these two factors, the pure phase stability was considered:

$$\left|g_{12\_PHASE}(\lambda)\right| = \left|\sum_{m\neq n} \exp\left\{-i\left[\arg\left(E_m(\lambda)\right) - \arg\left(E_n(\lambda)\right)\right]\right\}\right| \Big/ \left[N(N-1)\right] \tag{4}$$

where arg() is the argument of a complex number: arg[exp($i\varphi$)] = φ, $0 \le \varphi < 2\pi$. The pulse-to-pulse stability of spectral intensity is [16, 17]:

$$-C_v(\lambda) = -\sigma_I(\lambda)/\left\langle I_m(\lambda)\right\rangle = -\sqrt{\left\langle\left(I(\lambda)_m - \left\langle I_m(\lambda)\right\rangle\right)^2\right\rangle} \Big/ \left\langle I_m(\lambda)\right\rangle \tag{5}$$

in which C_v is the coefficient of variation, σ_I is the standard deviation of the spectral intensity, and $I_m(\lambda) = \left|E_m(\lambda)\right|^2$. The negative sign is used such that higher values of $-Cv$ correspond to higher stability. The maximum value of $-Cv$ is 0, which represents no pulse-to-pulse fluctuation in the spectral intensity. The evolution of $-C_v(\lambda,P)$ and spectrally-averaged $-C_v(P)$ were calculated similarly as the coherence evolution and the averaged coherence.

The results are shown in Fig. 4, along with the corresponding experimental results. Figures 4(a)–4(d) show power-dependent evolution for three fiber lengths, and Fig. 4(e) and 4(f) are spectrally-averaged coherence depending on the power. The simulated coherence shows qualitative agreement with the measurements, again confirming the association between coherence degradation and soliton fission.

There is some discrepancy in the wavelength range and the rate of coherence degradation, between measurements and simulations. For the shorter PCF lengths (4.7 mm and 3.9 mm), the measurements show quicker degradation at soliton fission than the simulations. This can be seen in the average coherence [comparing Fig. 4(e) with 4(f), i.e., the 4.7- and the 3.9-mm cases], and also in the evolution where the measurements show relatively abrupt drop of coherence, while the simulations show coherence degradation starting at the edges of the bandwidth and slowly spreading to larger ranges of wavelengths. For the 10.5-cm case, the average coherence drops to below 0.2 after soliton fission in the experiments, while to 0.6–0.4 in the simulations [comparing Fig. 4(e) with 4(f), i.e., the 10.5-cm case].

Optics EXPRESS

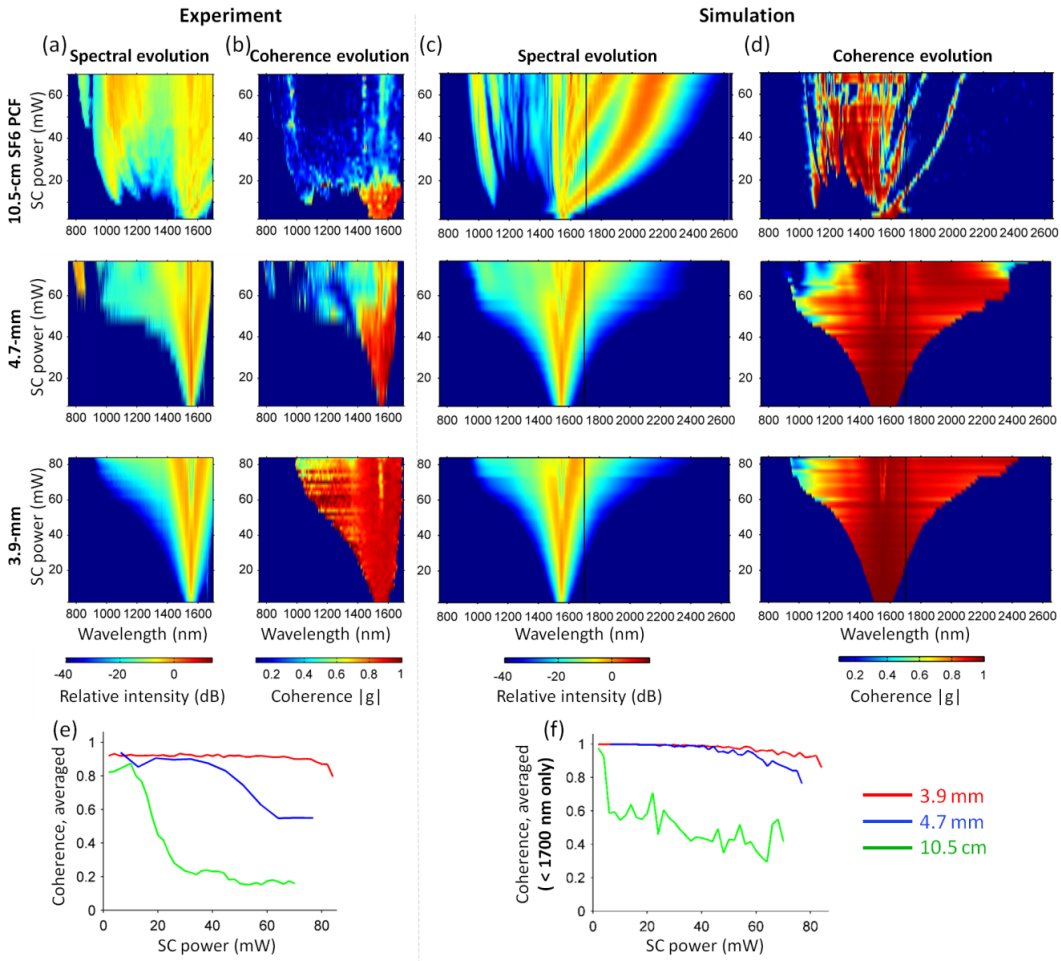

Fig. 4. Simulated coherence of SC generated in three different lengths of SF6 PCFs, in comparison with the experimental results. Column (a): three plots of measured spectral evolution using different fiber lengths. Column (b): measured coherence evolution. Column (c): simulated spectral evolution. Column (d): simulated coherence evolution. The simulation plots have black lines at 1700 nm to help visual comparison with the experimental results. In the experiment, radiation of relative intensity lower than about –40 dB was not measurable due to the sensitivity limitation; and in the simulations this part of radiation is also ignored. (e) and (f): spectrally-averaged coherence depending on the average SC power. In the simulations, shot noise and 5% pulse-to-pulse power fluctuation were added in the pump.

The coherence fluctuates in the regions where it starts to degrade. In the measurements, the fluctuation occurs along both the wavelength and the power axes [see Fig. 4(b), 3.9-mm case, below 1400 nm]. In the simulations, it occurs along the power axis [Fig. 4(d), both for the 4.7- and the 3.9-mm cases]. Generally, noise represents random fluctuation in the optical field, which causes degradation of coherence; in this case, fluctuation in the noise (e.g., having a different set of noise at each power) is suspected to cause fluctuation in coherence. To investigate this, GNLSE-based simulation are carried out at each power using a different (independently-generated) set of shot noise ($N = 20$ vectors of randomly-phased photons) and a different (independently-generated) set of pulse-to-pulse power fluctuation in the pump ($N = 20$ Δ_P's) [Fig. 5(b)]. To see whether different sets of noise are the cause of the coherence fluctuation, we tested using the same noise for all powers.

Optics EXPRESS

When using the same shot noise at all powers [Fig. 5(c), still using a different set of Δ_P's at each power], there is still fluctuation in the coherence. When using the same set of Δ_P's at all powers [Fig. 5(d) and 5(e) respectively, shot noise is still different at each power], the coherence fluctuation disappears. Comparing Fig. 5(d) with 5(e) indicates different sets of Δ_P's (shown in the histograms) yield different degradation of coherence. These results suggest that random Δ_P can be the cause of coherence fluctuation.

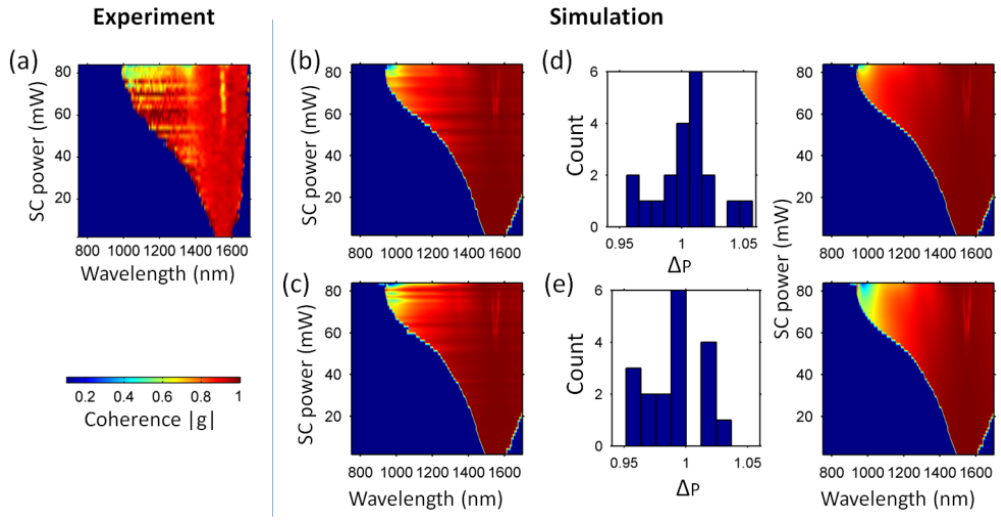

Fig. 5. (a) Measured coherence evolution for the 3.9-mm-fiber case. (b) Corresponding simulated coherence with different (independently-generated) noise at each power, including shot noise and the pulse-to-pulse power fluctuation in the pump (Δ_P). (c) Simulation results by using the same shot noise at all powers (the set of Δ_P's is still different at each power). (d) and (e): Two independent runs of simulation each using the same set of Δ_P's at all powers (shot noise is still different at each power). (d) and (e) each uses a same set of Δ_P's (as in the histograms), yielding no fluctuation in coherence, respectively. But (d) and (e) have different coherence between each other, since they use different sets of Δ_P's. These results show that random Δ_P can be the cause of the coherence fluctuation.

In the experiment, measurements were taken at one power after another, with spectral measurements obtained by scanning through wavelengths. Thus, each combination of power and wavelength sees a different set of Δ_P's, which causes coherence fluctuation along both the power and the wavelength axes. A possible improvement in the measurement could be obtained by single-shot spectral measurement, which would mitigate the coherence fluctuation along the wavelength axis.

Figures 5(d) and 5(e) show that two different sets of Δ_P's yield different coherence, with an ensemble size of $N = 20$. When N is large, the distribution consisting N random Δ_P's will approach the ideal normal distribution. In this case, any random set of Δ_P's will be nearly the same, causing the coherence fluctuation to be negligible. In the experiment, though, the value of N should not affect the fluctuation of coherence, since each pulse interferes only with the next one (one-pulse delay), unlike in the simulations where each pulse interferes with all others [$\langle\ \rangle_{m\neq n}$ in Eq. (3)].

Optics EXPRESS

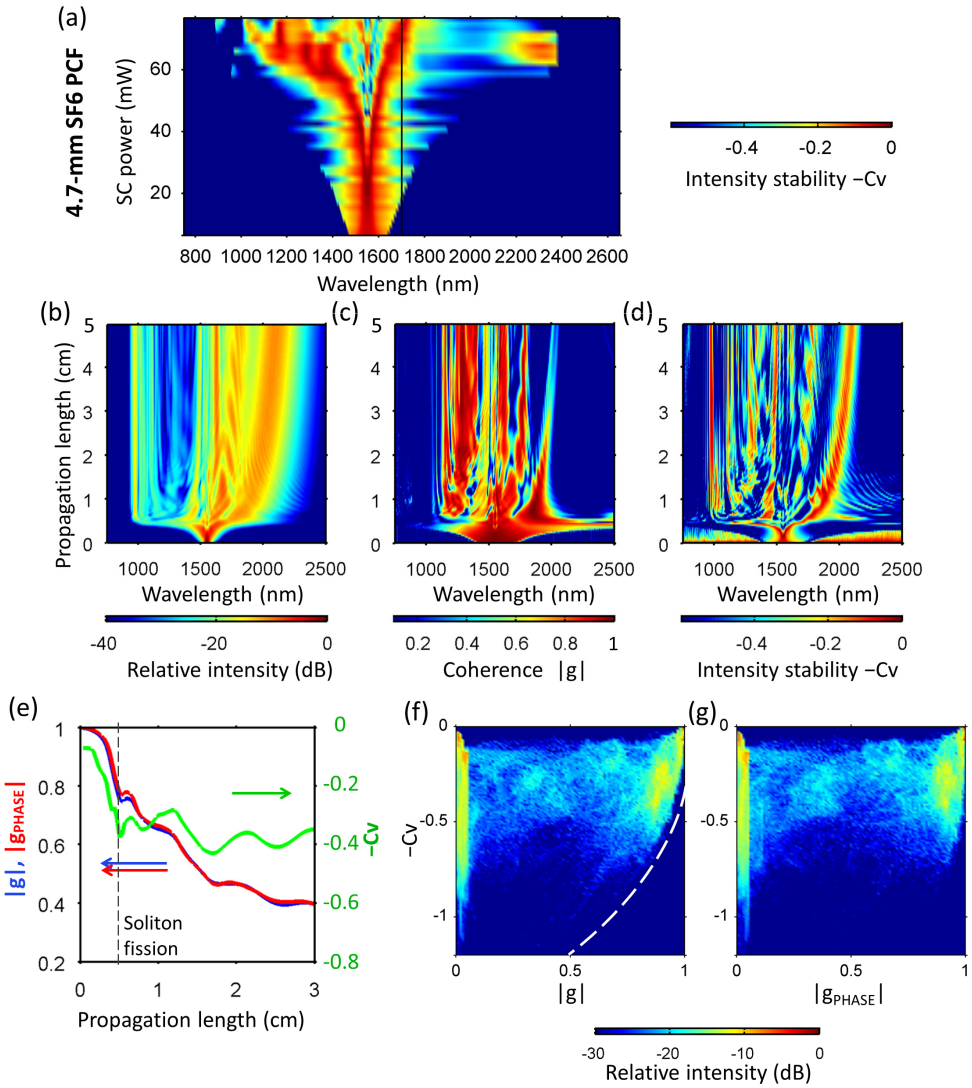

Fig. 6. Simulated pulse-to-pulse stability of spectral intensity (–*Cv*) and coherence. (a) Power-dependent evolution of –*Cv*, simulated with the parameters for the 4.7-mm SF6 PCF case. This can be compared with the 4.7-mm coherence evolution in Fig. 4(d). Similar to Fig. 4(d), radiation of relative intensity lower than about –40 dB is ignored. (b) The spectral evolution, (c) the evolution of coherence |*g*|, and (d) the evolution of –*Cv* depending on the propagation length, simulated using a 5-cm of same SF6 PCF and an average power of 70 mW. (e) Averaged coherence |*g*| (blue), phase stability $|g_{PHASE}|$ (red), and –*Cv* (green) depending on the propagation length. The soliton fission length (4.8 mm) is marked with a dashed line. (f) Distribution of SC power as a function of |*g*| and –*Cv*, (g) distribution of SC power as a function of $|g_{PHASE}|$ and –*Cv*. (f) and (g) concern the radiation at all the lengths in (b). (g) shows low correlation between –*Cv* and $|g_{PHASE}|$. (f) shows similar trends except for a forbidden area to the right-bottom of the dash curve, because –*Cv* is coupled in |*g*|.

The pulse-to-pulse stability of spectral intensity –*Cv* and the coherence |*g*| both quantify SC stability, and might be expected to show similar trends. –*Cv* is coupled in the definition of the coherence [Eq. (3)], and makes a minor contribution in determining the coherence [1]. In our simulations, the overall –*Cv* is not always highly correlated with the overall coherence |*g*| or with the pulse-to-pulse stability of spectral phase $|g_{PHASE}|$ [defined in Eq. (4)]. Also, spectral components with high/low –*Cv* do not have correspondingly high/low |*g*| or $|g_{PHASE}|$.

Optics EXPRESS

Figure 6(a) is the simulated power-dependent evolution of $-Cv$ using the parameters of the 4.7-mm SF6 PCF. Comparisons with the simulated coherence evolution [Fig. 4(d), 4.7-mm case] show that $-Cv$ starts degrading earlier than the coherence. High (close to 0) $-Cv$ is maintained only along the red "Y shape" [see Fig. 6(a)] which is the pump peak and the peaks of the two spectral lobes that the pump peak splits into. This is similar to previously reported results in the picosecond regime [17]. Comparing the evolution along the propagation length [Fig. 6(c) vs. 6(d)] and comparing the average values along the propagation length [Fig. 6(e)] also show that $-Cv$ starts degrading earlier than the coherence. Figure 6(e) further shows that $-Cv$ stays relatively stable after soliton fission (marked by a dash line), while the coherence $|g|$ and the phase stability $|g_{PHASE}|$ continue to degrade.

4. Conclusions

Spectral and coherence evolution were experimentally measured for SC generated in different lengths of highly nonlinear SF6 PCFs to visualize the pulse-to-pulse coherence of SC. Numerical simulations were carried out to accompany the measurements.

The spectral evolution measurement allows for detailed feature comparisons between simulation and experiment which promises to be an interesting source of insight for future investigation on the interplay between pulse noise, stability, and random pulse-to-pulse fluctuation and its effect on the spectral properties of SC.

The measurements and the simulations show qualitative agreement in the coherence, and both confirm the association between coherence degradation and the onset of soliton fission. The experiments and the simulations both show fluctuation in the coherence in correspondence to the onset of higher-order nonlinear effects present in the fiber. This observation underscores the richness of the nonlinear phenomena observed in highly-nonlinear pulse transformation in fibers and the critical dependence between source and output radiation for SC applications.